Title

A computational assessment of the electronic, thermoelectric, and defect properties of bournonite (CuPbSbS 3) and related substitutions

Journal

Physical Chemistry Chemical Physics, 19(9)

ISSN

1463-9076

Authors

Faghaninia, Alireza
Yu, Guodong
Aydemir, Umut
et al.

Publication Date

2017-03-01

DOI

10.1039/c7cp00437k

Peer reviewed

A computational assessment of the electronic, thermoelectric, and defect properties of bournonite ($CuPbSbS_3$) and related substitutions

Alireza Faghaninia[†,*], Guodong Yu[¶], Umut Aydemir[§], Max Wood[§], Wei Chen[¶], Gian-Marco Rignanese[¶], G. Jeffrey Snyder[§], Geoffroy Hautier[¶], and Anubhav Jain[†,*]

† Energy Technologies Area, Lawrence Berkeley National Lab, 1 Cyclotron Rd, Berkeley, CA, USA

§ Department of Materials Science and Engineering, Northwestern University, 2220 Campus Drive, Evanston, IL, USA

¶ Institute of Condensed Matter and Nanosciences (IMCN), Université catholique de Louvain, Chemin des étoiles 8, bte L7.03.01, Louvain-la-Neuve, Belgium

ABSTRACT

Bournonite ($CuPbSbS_3$) is an earth-abundant mineral with potential thermoelectric applications. This material has a complex crystal structure (space group $Pmn2_1$ #31) and has previously been measured to exhibit a very low thermal conductivity (κ<1 W/m·K at $T\geq$300 K). In this study, we employ high-throughput density functional theory calculations to investigate how the properties of the bournonite crystal structure change with elemental substitutions. Specifically, we compute the stability and electronic properties of 320 structures generated via substitutions {Na-K-Cu-Ag}{Si-Ge-Sn-Pb}{N-P-As-Sb-Bi}{O-S-Se-Te} in the $ABCD_3$ formula. We perform two types of transport calculations: the BoltzTraP model, which has been extensively tested, and a newer AMSET model that we have developed and which incorporates scattering effects. We discuss the differences in the model results, finding qualitative agreement except in the case of degenerate bands. Based on our calculations, we identify *p*-type $CuPbSbSe_3$, $CuSnSbSe_3$ and $CuPbAsSe_3$ as potentially promising materials for further investigation. We additionally calculate the defect properties, finding that *n*-type behavior in bournonite and the selected materials is highly unlikely, and *p*-type behavior might be enhanced by employing Sb-poor synthesis conditions to prevent the formation of Sb_{Pb} defects. Finally, we discuss the origins of various trends with chemical substitution, including the possible role of stereochemically active lone pair effects in stabilizing the bournonite structure and the effect of cation and anion selection on the calculated band gap.

1 Introduction

Thermoelectric (TE) devices based on solid-state materials have the potential to contribute solutions to the current energy dilemma. Thermoelectric technology can be used for power generators, Peltier coolers or other applications such as embedded active

cooling in microprocessors, infrared detectors, and optoelectronics.[1,2] All these applications require high performance thermoelectric materials to be cost-competitive. The efficiency of a thermoelectric material is determined based on the dimensionless figure of merit, zT, defined as $zT = \frac{\alpha^2 T}{\rho\kappa}$, where α, ρ and κ correspond to the Seebeck coefficient, electrical resistivity, and thermal conductivity, respectively. Enhancing a material's zT is not trivial as most of these transport coefficients are interdependent. Except for κ_L, all other terms are greatly affected by the charge carrier concentration.[3] Hence, to optimize zT, the carrier concentration must be tuned and κ_L should be lowered. Reduction of κ_L can be engineered by introducing various phonon scattering sources such as nanoparticles, grain boundaries, and point defects.[4] Furthermore, some materials such as clathrates[5], skutterudites[6], Sb-based Zintl phases[7,8], 1-1-2 chalcogenides[9,10] or $Cu_{2-x}Se$[11] inherently possess very low thermal conductivities. Other copper selenides such as $Cu_3Ge_ySb_{1-y}Se_{4-x}S_x$ and Cu_3SbSe_4 were also investigated as high-performing TE materials with thermal conductivity as low as 0.5-2 W/m·k and zT values as high as 0.8.[12,13] Tuning the electronic properties of compounds identified to exhibit a low κ_L is one route towards designing improved thermoelectric materials.

Traditionally most thermoelectric materials are prepared using high purity elements, which can be very costly and energy intensive. Recently, naturally occurring minerals (*e.g.*, tetrahedrites, argyrodites, bornites, colusites) have attracted increasing attention in thermoelectric research as some have been demonstrated to possess competitive zTs (*e.g.*, $zT_{bornite}$ = 1.2 at 900 K ; $zT_{tetrahedrite}$ = 1.0 at 723 K ; $zT_{argyrodite}$ = 1.1 at 723 K; $zT_{colusite}$ = 0.73 at 663 K).[14–17] In addition to being less energy intensive to form, many naturally occurring minerals are composed of non-toxic and earth-abundant elements, which are better alternatives to common TE materials composed of toxic or scarce elements (*e.g.*, Pb, Te, As, Ge). Ultralow thermal conductivities (κ < 1 W/mK) is a common feature of these investigated minerals.[14–19] For example, Morelli et al. revealed that for tetrahedrites, there is a correlation between the glassy behavior of thermal conductivity and the Sb lone pairs, inducing strong lattice anharmonicity in the phonon spectra (leading to large Grüneisen parameter).[16,18] In addition, argyrodite is known for its superionic behavior due to the interaction of mobile cations and vacancies leading to extremely low thermal conductivities.[14–19]

This paper focuses on the mineral bournonite ($CuPbSbS_3$), which is found in sulfide ore deposits. Bournonite crystallizes in a noncentrosymmetric orthorhombic lattice (space group $Pmn2_1$).[20] The crystal structure of the mineral can be related to stibnite, Sb_2S_3, in which Pb and Sb atoms possess mixed occupancy on the Sb site (2*a*) and Cu atoms fill tetrahedral voids (in the 4*b* site) in the Sb_2S_3 lattice. A previous description of bournonite by Bairamova et al. indicated that Pb atoms can be substituted by Eu and Yb, and that Sb atoms could be substituted by La and Nd in the crystal structure, indicating a certain

degree of chemical flexibility.[21] Although they measured a Seebeck coefficient as high as 480 uV/K at 560 K, the thermoelectric performance was hindered by a low intrinsic electrical conductivity.[21] Magnetic measurement on $PbCuSbS_3$ nanocrystals fabricated by Wei et al.[22] indicated diamagnetic behavior; furthermore, they measured an optical band gap of 1.3 eV as well as the heat capacity. Dong et al.[23] indicated that stereochemically active lone-pair s^2 electrons are a source of anharmonic phonon scattering resulting in the thermal conductivity as low as 0.81 W/m·K at 300 K and 0.48 W/m·K at 600 K in bournonite and also suggested thermoelectricity as a potential application of bournonite.[23]

In this paper, we use high-throughput density functional theory (DFT) to investigate the formation energy, energy above hull, band gap, and maximum *n*-type and *p*-type power factor (PF) of 320 compounds that are generated via substitution of elements in natural mineral bournonite. We have two goals for this study. Our applications driven goal is to identify novel compositions in the bournonite structure that exhibits promising thermoelectric properties and is close to thermodynamic stability, *i.e.*, possibly synthesizable. Our scientific goal is to systematically describe how changing composition within the fixed bournonite crystal structure affects various thermodynamic and electronic properties. For this latter goal, we aim to eventually contribute new chemical principles for designing thermoelectric materials.[24–26] High throughput DFT and electronic transport properties computations are a unique tool because they allow one to rapidly generate large data sets that offer independent control over chemistry and structure, making it possible to separate out factors in a way that is difficult to achieve experimentally.[26–36]

2 Methods

There are several types of calculations that are performed in this study:

1. High-throughput DFT band structure and uniform non self-consistent calculations.

2. Transport properties calculations by two software packages: BoltzTraP[37] and the ab initio model for mobility and Seebeck coefficient (AMSET[38], previously called aMoBT).

3. DFT calculation of necessary inputs for AMSET code such as phonon frequencies, static and high-frequency dielectric constants, and average deformation potential.

4. Defect formation energy calculations and spin-orbit coupling calculations for candidates that may be promising thermoelectrics.

We describe the methodology used for each of these calculation types separately.

2.1 High-throughput DFT calculations

We performed the DFT calculations using Vienna ab initio Simulation Package (VASP[39,40]) with the exchange-correlation functional of Perdew-Burke-Ernzerhof

(PBE)[41] generalized gradient approximation (GGA) and projector augmented-wave (PAW)[42,43] pseudopotentials. We use an energy cutoff of 520 eV; increasing the cutoff to 700 eV changes the total energy of the bournonite lattice only by 7.0×10^{-4} eV/atom. Furthermore, restricting the energy convergence criterion to 10^{-5} eV rather than 1.2×10^{-3} employed, changes the total energy only by 1.6×10^{-6} eV/atom. The calculations involve structure optimization, self-consistent field charge density optimization and two non-self-consistent steps: one line-mode band structure and one in dense uniform k-point mesh for transport properties calculations. All these steps are performed automatically through the atomate software package (https://github.com/hackingmaterials/atomate) which employs the FireWorks[44] workflow software package to automatically run, repair (via the custodian package, (https://github.com/materialsproject/custodian) and report back the status and the outcome of the calculations in a MongoDB database format. In addition, atomate employs the pymatgen[45] package to organize inputs and output files and to perform analysis such as band structure plotting or extracting data from BoltzTraP.

Overall, we calculate and analyze in a high-throughput manner:
1. The formation energy per atom, E_{form} (eV)
2. The energy above hull per atom, E_h (eV)
3. The band gap, E_g (eV)
4. *n*-type power factor, *n*-PF ($\mu W/cm\cdot K^2$)
5. *p*-type power factor, *p*-PF ($\mu W/cm\cdot K^2$)

Calculating E_{form} is straightforward from DFT energies; for example, E_{form} of $AgPbNSe_3$ is $[E(AgPbNSe_3) - E(Ag) - E(Pb) - \frac{1}{2}E(N_2) - 3E(Se)]/6$ where E() is the DFT total energy. However, a major issue with the formation energy as a thermodynamic stability measure is that most compounds do not decompose into their component elements. A more accurate procedure is to evaluate the energy of the most energetically favorable decomposition, which could include a mix of elements, binaries, ternaries, or higher order compounds. A large decomposition energy, or "energy above hull", will indicate a thermodynamically unstable compound. Calculating the energy above hull requires knowledge of the energies of all compounds that could be made from any combination of the starting elements. To obtain a good approximation to this data, we use all compounds in the Materials Project[46] database. More details on this method and comparison with experimental data is available elsewhere.[47,48] The electronic band gap, Eg, reported in eV is a well known characteristic of the band structure. The thermoelectric power factors, n-PF and p-PF, are the electronic part of the figure of merit, zT, defined as $\sigma\alpha^2$ where σ and α correspond to electrical conductivity and Seebeck coefficient respectively. The PF quantifies the amount of electrical power that can be generated via a TE material in a limited physical space. We present this quantity in units of $\mu W/cm\cdot K^2$. We note that a

power factor of 30 $\mu W/cm \cdot K^2$ at T = 600 K is equivalent to $zT = 1.8$ if we assume $\kappa = 1$ W/m·K.

Inspired by Zeier et al.[24], for interpretation of the data, we look at atomic and ionic radii, electronegativity, and bonding environments. The coordination numbers (CNs) have been calculated using the chemenv environment in pymatgen.[45] We employed the SimplestStrategy with a distance_cutoff of 1.4 and an angle_cutoff of 0.3 to automatically calculate the CNs for all the species in all the structures. It should be noted that for each species, we average the calculated CNs for all the sites; we report this averaged CN which may be a non-integer. For example, the CN of Pb (considering both neighboring S and Cu atoms) is 8.5 which is consistent with 8 for one site and 9 for the other as reported previously[23]; other calculated CNs for bournonite also match previous reports. Calculated CNs are available in the spreadsheet in the Supporting Information.

We used pymatgen's StructureMatcher[45] tool to analyze whether the substituted structures maintained the general lattice shape and local structure motifs of the prototype bournonite structure within an affine transformation mapping. The parameter bounds for the affine transformation and local atomic position matching were length tolerance=0.2, angle tolerance=5, and site tolerance=0.3. For spacegroup analysis, we use an adapter to the spglib library (http://atztogo.github.io/spglib/) as implemented in pymatgen.

2.2 Transport properties calculations

The conductivity and Seebeck coefficient (and therefore the power factors) of the substituted structures have been calculated using two techniques. The first calculation method is theBoltzTraP code[37] within the constant relaxation time approximation which is set to $\tau = 10^{-14}$ s; this arbitrary value is intended for the purposes of qualitatively ranking compounds rather than explicit and accurate prediction of the conductivity. In a previous work, we tested the accuracy of BoltzTraP in computing these quantities over various compounds, finding that the Seebeck coefficient is generally reproduced well but the power factor is difficult to estimate within a global relaxation time approximation.[29] In addition, the known[49,50] underestimation of GGA band gaps further reduces the accuracy of BoltzTrap calculations from GGA band structures, particularly for low-gap (*i.e.*, <0.2 eV) compounds.[29] Nevertheless, BoltzTrap is powerful in that it only requires a band structure as an input, takes into account anisotropy and multivalley effects, and has been well-tested by the community. The second calculation method we use is the AMSET package.[38] The major advantage of AMSET is that it does not assume a relaxation time. Instead, it accounts for different scattering mechanisms such as acoustic and optical phonon scattering as well as ionized impurity scattering. The AMSET method requires the knowledge of some materials parameters such as static and high-frequency dielectric constants and phonon frequencies, which we determine fully *ab initio* (as explained in section 2.3). AMSET also models inter-band scattering of the heavy and the

light band, which is known to reduce the electrical mobility.[51,52] A disadvantage of AMSET is that it currently uses a one-dimensional model of the averaged band structure for a single pocket, which cannot capture anisotropy and may be less accurate for multivalley compounds. Previous work indicates that, compared with BoltzTrap, AMSET offers more accurate prediction of mobility and almost identical or slightly better accuracy in predicting the Seebeck coefficient.[38] However, for the reasons mentioned above, we use both of these models for screening and narrowing down the choices of promising TE candidates.

The thermal conductivity, κ, of bournonite has been measured to be lower than 1 W/m·K at room temperature and decreases even further at higher temperatures.[23] Furthermore, Sb (more generally group 15, s^2 lone-pairs) exhibits a causal relationship with low thermal conductivity in bournonite[23,53], and our substitutions always have one element from group 15 included. Therefore, we focus on the electronic properties of these substitutions expecting thermal conductivities to be generally low when such lone pairs are present.

2.3 Parameter calculations

The force constants have been calculated using density functional perturbation theory (DFPT) and the phonopy[54] package is used to calculate the phonon density of states (DOS) at the Γ point. The peak with the highest frequency in the phonon DOS has been selected as the longitudinal optical (LO) phonon frequency used in AMSET.

The dielectric constants have been calculated using DFPT in VASP. Petousis et al.[55] have demonstrated that this method is relatively accurate, *i.e.*, within 25% of the experimental measurements for most calculated data. Furthermore, Bahers et al.[56] demonstrated that GGA-PBE functional is relatively accurate in calculating the static and high frequency dielectric constants. We calculate the static dielectric constant by summing the electronic contribution including local field effects and the ionic contribution. At high frequencies where the ionic contribution goes to zero, we approximate the high frequency dielectric constant as equal to only the electronic component. We note that a second way of calculating the high frequency dielectric constant (not used in this work) is to use the calculated static dielectric constant and the LO and TO phonon frequencies and estimate the value of the high-frequency dielectric constant using the Lyddane-Sachs-Teller relation.[57] We also calculate the conduction and the valence band volumetric averaged deformation potentials as described by Faghaninia et al.[38] and Rode.[58] It should be noted that regardless of the value calculated for this parameter or elastic constants, acoustic phonon deformation potential scattering does not limit the mobility in bournonite or its substitutions, hence the value of the deformation potential and elastic constant have a negligible effect on the AMSET calculated values for this specific group of materials.

2.4 Defects calculations

We use a 2x2x1 supercell with a 2x2x2 grid of k-point. A total energy convergence criteria of 0.001 eV is used for the relaxation of structures. The formation energy of defect D in q charge state is calculated through the following equation[59]:

$$E_{df}[D^q] = E[D^q] - E[bulk] - \sum_i n_i \mu_i + qE_F + E_{corr}[D^q]$$

Here, $E[D^q]$ and E[bulk] are the total energies of the supercell with the defect D in q charge state and without any defect (bulk), respectively. n_i is the number of removed ($n_i<0$) or added ($n_i>0$) i-type atoms, and μ_i is their chemical potential. E_F is the Fermi energy (chemical potential of the electrons) relative to the valence band maximum. $E_{corr}[D^q]$ are the corrections for the spurious image-image interaction and potential alignment.

The chemical potential of elements were obtained from stable region (E_h = 0 eV) of the phase diagram supported by all corresponding compounds extracted from Materials Project database using the pymatgen package.[45] For a stable compound, the regions in which the chemical potentials are calculated should include the compound itself. However, for unstable structures (E_h > 0 eV), it should include all the compounds that the structure would decompose to. Before applying the corrections, we verify the localization of a charged defect state by checking its wave function. Then, the localized charged defect states are corrected by the extended Freysoldt scheme of Kumagai et al..[60,61] For delocalized defects, only the potential alignment between the bulk and neutral state was included.

2.5 Data completeness

The calculated data for structures, formation energy, band gaps as well as the energy above hull are complete for all 320 substitutions. There are 9 missing BoltzTraP calculations; however, these compounds do not have a low enough E_h to be reported to Table 1. Furthermore, 61/320 of the AMSET calculations are missing due to various problems in converging the necessary parameter data. However, none of these have a low enough energy above hull to affect our discussion based on Table 1. Workflow managements software packages such as atomate or FireWorks are not used for AMSET calculations unlike the rest of the calculations in this paper. See the spreadsheet in Supporting Information for more details.

3 Results

3.1 Crystal Structures

$CuPbSbS_3$ (bournonite) has a relatively complex structure. It crystalizes in a fairly large (volume: 555 $Å^3$) orthorhombic unit cell with the space group $Pmn2_1$ (number 31).

Because 319 out of 320 substitutions retain the same space group even after DFT structure optimization, we use Figure 1 to describe the structure of the entire $ABCD_3$ group where *A*: {Na, K, Cu, Ag} and *B*: {Si, Ge, Sn, Pb} and *C*: {N, P, As, Sb, Bi} and *D*: {O, S, Se, Te}. The only exception to the orthorhombic $Pmn2_1$ symmetry is $AgSiSbO_3$ which relaxes to *Pnma* (number 62) structure but it is highly unstable (E_h = 0.489 eV). The number of formula unit per cell is 4 for all 320 structures (i.e. 24 atoms in each structure). We acknowledge that Na/K and Cu/Ag belong to different groups of the periodic table but for simplicity we consider them in the same group, *A*, as they all have a +1 oxidation state. However, we analyze them separately when necessary.

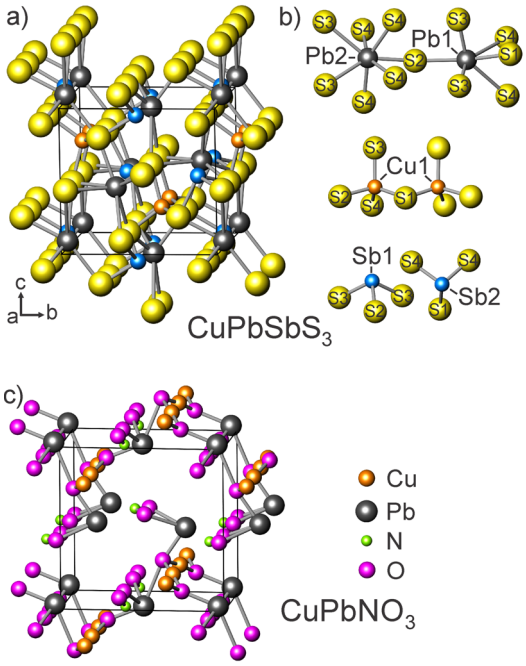

Figure 1. (a) Crystal structure $CuPbSbS_3$ (b) The local bonding environments of $CuPbSbS_3$: Pb neighbors 6 and 7 S atoms, with Cu in tetrahedral and Sb in trigonal pyramid coordination environments. (c) Crystal structure of DFT-optimized $CuPbNO_3$: the bournonite-type structure is not retained upon cell and atom position optimization, even though the spacegroup number (31) remains the same.

Several copper and silver chalcogenides with the general $ABCD_3$ formula have been previously synthesized such as the cubic $AgPbSbSe_3$, $AgSnSbS_3$ and monoclinic $AgPbSbS_3$, $AgPbAsS_3$, $CuSnAsSe_3$, $CuSnSbSe_3$ and triclinic $AgSnAsS_3$ by Kheifets et al.[62] or high-pressure (<45 GPa) cubic $AgGeSbSe_3$, $AgSnSbS_3$, $AgPbSbSe_3$ and monoclinic $AgGeAsS_3$, $AgGeSbS_3$, $AgPbAsS_3$, $AgPbAsSe_3$ and triclinic $AgSnAsS_3$ reported by Kheifets et al.[63]. However, it should be stressed again that here we only focus on bournonite $ABCD_3$ substitutions that crystallize only in orthorhombic $Pmn2_1$ structure.

Figure 1 depicts the crystal structure of bournonite. In bournonite, Cu atoms reside in the tetrahedral site neighboring 4 S atoms. One of the two Sb sites, Sb1, form a trigonal

pyramid with 3 S atoms (one S2 and two S3) and the other, Sb2, forms another trigonal pyramid with 3 S atoms (one S1 and two S4). The trigonal pyramid arrangement suggests a lone pair state, as is observed in electron localization function calculations by Dong et al.[23] Pb also occupies two crystallographic sites: one Pb1 atom surrounded by six S atoms (distorted octahedron) and Pb2 with seven S atoms (monocapped trigonal prism).[23] The distorted nature of these environments are also suggestive of a second lone pair behavior.

All substitutions result in 320 structural configurations (simply $4\times4\times5\times4$). These structures are all initialized with the same lattice constants of a = 7.81 Å, b= 8.16 Å and c = 8.71 Å (cell volume ~ 555.1 Å^3) consistent with previous reported values[23,64] for bournonite. For $CuPbSbS_3$, the lattice constants expanded to a = 7.86 Å, b = 8.29 Å and c = 9.03 Å (~588.4 Å^3). This magnitude of expansion compared with experimental values is typical of the GGA-PBE functional, which is known to underbind.

We categorize the structures as "bournonite-type" if the final/relaxed structure is similar to that of bournonite in terms of cell shape and atom positions as determined by the StructureMatcher tool in pymatgen. The difference between "bournonite-type" and "non-bournonite" type structures is plotted in Figure 1-c using $CuPbNS_3$ as an example of the former and $CuPbNO_3$ as an example of the latter. As illustrated in Figure S1, a compound containing K almost never relaxes to a bournonite-type structure because the large size of K blocks other elements from bonding in the desired arrangement. Compounds containing O or N also form bournonite-type structures much less frequently than other elements. As we describe later, substitutions that retain the bournonite structure are more directly comparable and the trends are more clear.

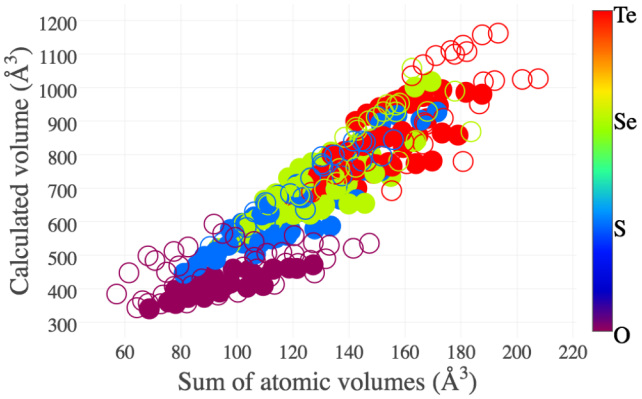

Figure 2. The DFT optimized volume plotted against the sum of atomic volumes determined by the composition (both in Å^3). The colors separate compounds based on their anion. The overall volume is to a large extent determined by the size of their constituent atoms. Filled markers indicate that the structures are similar to bournonite while the open markers are structures relaxed to non-bournonite arrangements.

The cell volumes of the substituted structures vary greatly, ranging from 339.9 Å^3 for

$CuGePO_3$ to 1162.6 $Å^3$ for $KSnBiTe_3$. The calculated values of lattice parameters are presented in the spreadsheet provided in Supporting Information. The cell volumes are largely determined by the sum of atomic volumes of the individual elements for each site, as plotted in Figure 2. The overall correlation coefficient between sum of atomic volumes and calculated cell volumes for all the structures is 0.90. Stated another way, the packing fraction of bournonites falls within a well-defined range, with a mean centered at 0.192 with a standard deviation of 0.027. We note that, for oxides, the sum of atomic volumes appears to be less deterministic (Figure 2) and cell volumes overall fall within a smaller range of values. Furthermore, we note that using atomic volumes based on ionic radii (when available) rather than atomic radii did not improve the level of agreement with the calculated cell volumes.

3.2 Potential thermoelectric materials

To evaluate the feasibility of our tested substitutions as thermoelectric materials, we compare their electronic transport properties. Later, we discuss the results of defect formation energy calculations for a few selected compounds to identify mechanisms that limit dopability and narrow down our search for high-performing substitutions with the potential for synthesis.

3.2.1 Transport properties

We calculate the Seebeck coefficient and mobility/conductivity of all 320 structures via BoltzTraP and AMSET. To focus our search on compounds with the greatest chance of successful synthesis in the bournonite structure, we present the ten compounds with the lowest energy above hull, E_h, (i.e., most stable) in Table 1, where *n*-PF (*n*-type power factor) and *p*-PF are calculated with BoltzTraP at the fixed carrier concentration of $c = 10^{20}$ cm^{-3} and T = 600 K to compare the candidates at reasonable doping and operating conditions. For these calculations, we assume a constant relaxation time of $\tau = 10^{-14}$ s across all temperatures and carrier concentrations. We emphasize again that this assumption is intended for the purposes of qualitatively ranking compounds rather than explicit and accurate prediction of the conductivity. We acknowledge the limitations of such assumptions when the calculated properties are compared with experiment as discussed elsewhere.[29,38] As a second method to compare power factors, $n\text{-PF}^*/p\text{-PF}^*$ are calculated via AMSET. We note that the calculated power factors via AMSET, PF^*, are different and generally higher than those calculated via BoltzTraP; we will discuss this further in the Section 4.

Formula	E_h	E_g	*n*-PF	*p*-PF	$n\text{-PF}^*$	$p\text{-PF}^*$
$CuPbAsS_3$	0.001	0.53	5.7	12.5	19.5	20.7
$CuPbSbS_3$	0.002	0.69	5.3	13.8	18.8	21.5
$AgPbAsS_3$	0.010	0.83	6.6	13.4	24.1	13.8
$CuPbAsSe_3$	0.010	0.46	6.3	12.3	27.4	29.5
$CuSnSbS_3$	0.011	0.60	3.9	17.3	12.6	0.5

$CuSnAsS_3$	0.014	0.74	2.2	12.9	18.2	1.2
$CuPbSbSe_3$	0.016	0.36	3.2	14.2	14.5	27.7
$CuSnSbSe_3$	0.016	0.20	2.2	12.9	18.2	34.0
$AgSnAsSe_3$	0.017	0.66	18.1	12.1	28.2	32.8
$CuSnAsSe_3$	0.020	0.27	4.9	12.3	30.9	33.1

Table 1. Calculated properties for the most stable bournonite substitutions. n-PF and p-PF are the power factors calculated by BoltzTraP at the carrier concentration of c=10^{20} cm^{-3} and temperatures, T= 600 K. n-PF* and p-PF* are calculated via AMSET at the same c and T. PFs are in $\mu W/cm \cdot K^2$, E_g in eV and E_h in eV/atom.

Among the materials presented in Table 1, $CuPbAsS_3$ and $CuPbSbS_3$ and possess the lowest E_h which is consistent with previous reports of their synthesis.[20,23] These two compounds exhibit comparable electronic properties. Other interesting compounds with relatively favorable E_h of 0.010 eV are $AgPbAsS_3$ and $CuPbAsSe_3$. In particular, $CuPbAsSe_3$ has a p-PF* (asterisk means PF is calculated via AMSET) greater than $CuPbSbS_3$. We discuss the differences in the two models (p-PF vs p-PF*) further in Section 4. For example, p-PF* is low compared with p-PF for CuSnSbS3 and CuSnAsS3 due the inter-band scattering that is considered in AMSET, resulting in a much lower predicted mobility. We note that our focus on p-type behavior is based on defect analysis (demonstrated later in this manuscript), which indicates that n-type doping of bournonite compounds is unlikely due to electron killers (B-site vacancies, particular for Pb-based compounds).

For the remainder of our analysis, we narrow down our choices to relatively stable compounds with earth abundant elements in them which have a high calculated p-PF*. We identify three such candidates: $CuPbSbSe_3$, $CuSnSbSe_3$ and $CuPbAsSe_3$. To our knowledge, $CuPbSbSe_3$ is a novel compound that is yet to be synthesized and $CuSnSbSe_3$ has only been reported[62] in the monoclinic phase (i.e., not bournonite). Although $CuPbAsSe_3$ contains arsenic, which is non-ideal for practical application, its defect and band structure properties are favorable for TE applications. We pursue defects calculations for these candidates in Section 3.2.2. We also discuss the band structures and power factors in Section 4. As previously mentioned, Kheifets et al.[62] reported high-pressure synthesis of monoclinic $CuSnSbSe_3$. We also calculated the p-PF and p-PF* of this compound to be 18.7 and 1.8 $\mu W/cm \cdot K^2$ respectively.

3.2.2 Defects

The calculated formation energy versus Fermi level plots for intrinsic defects of $CuPbSbS_3$, $CuPbSbSe_3$, $CuSnSbSe_3$ and $CuPbAsSe_3$ are presented in Figure 3. All of these compounds are susceptible to acceptor (electron killer) defects (e.g., V_{Pb}, Cu_{Pb}, Sn_{Sb}…) with negative formation energies at the Fermi levels close to the CBM. These acceptor defects will act as electron-killers and impede n-type doping.[65] Although we have not explicitly calculated the defect formation energy of all possible bournonite substitutions, we expect that some type of acceptor vacancies will persist throughout the

series of bournonite compounds (see Figures S6-S8 for vacancy formation energies at all chemical potentials). Therefore, it will be extremely difficult to dope these materials *n*-type and they are expected to all exhibit intrinsic *p*-type behavior. Therefore, we focus on *p*-type dopability of these compounds and we report in Figure 3. the defect energy levels at the region of the phase diagram that result in the most favorable acceptor energy levels.

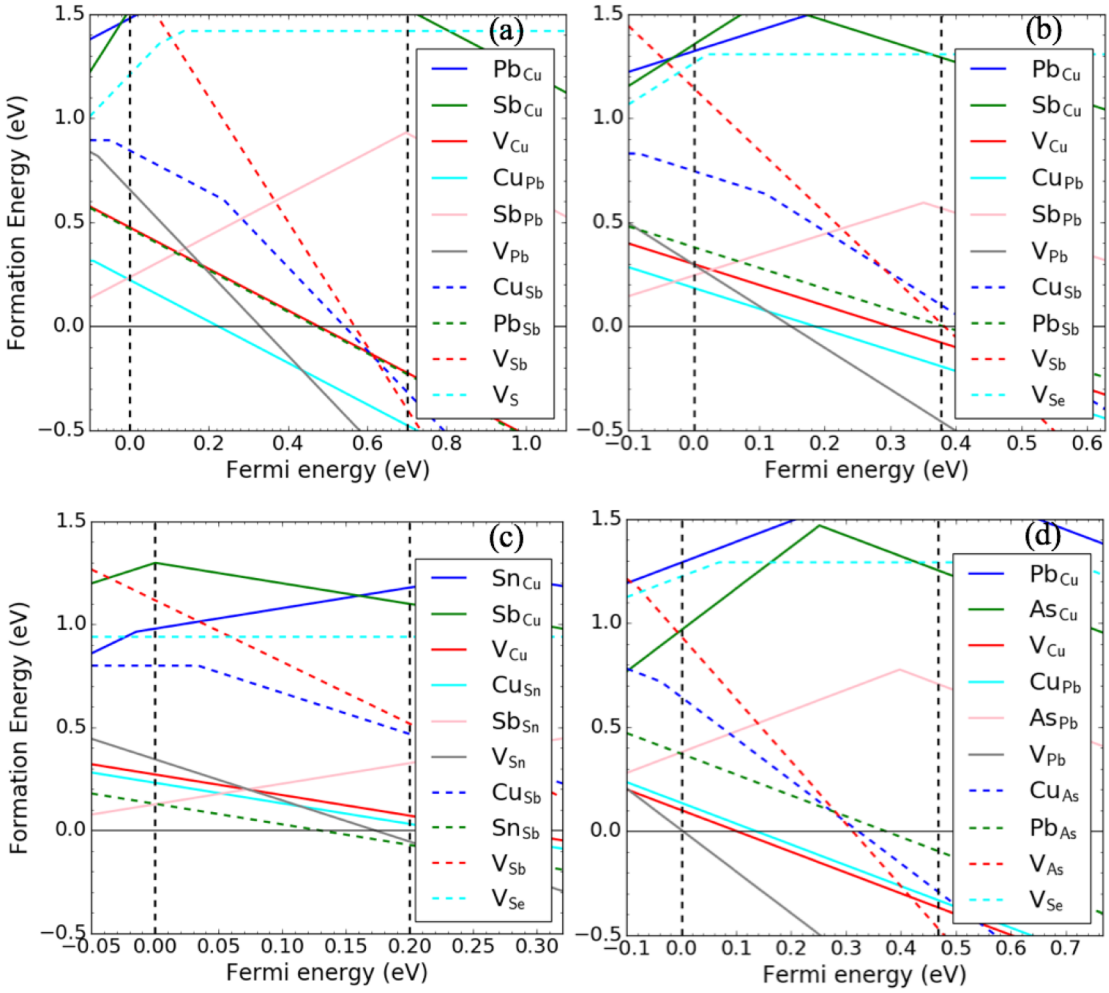

Figure 3. Formation energies of intrinsic defects for a) $CuPbSbS_3$, b) $CuPbSbSe_3$, c) $CuSnSbSe_3$ and d) $CuPbAsSe_3$. The chemical potentials (values are listed in the supporting information) are taken from a single region of the phase diagram that results in the lowest energy for shallow acceptors (Cu_{Pb}, Cu_{Pb}, Sn_{Sb} and V_{Pb}, respectively) in order to optimize *p*-doping. The two dashed vertical lines represent the VBM and CBM. All three a, b, c diagrams indicate strong *p*-type preference with potential for enhancement through Sb-poor synthesis. Defect diagram of $CuPbAsSe_3$ shows strong intrinsic *p*-type characteristic. See Figures S6-S13 for further diagrams containing both the intrinsic defects at all chemical potentials as well as extrinsic defects for $CuPbSbS_3$.

The main acceptors close to the VBM of bournonite (Figure 3-a) are Cu on Pb site (Cu_{Pb})

followed by Cu vacancies (V_{Cu}) while the main donor (hole killer) at that level is Sb on Pb site. A Fermi level, E_F, at the VBM or lower (inside the valence bands) is favorable as it results in high hole concentrations and favorable thermoelectric properties as presented in Table 1. However, at Sb-rich condition (Figure S6), at or below this level the formation of hole killers is more energetically favorable than acceptors which results in Fermi level pinning, maintaining E_F higher than the VBM. This is likely to result in low intrinsic hole concentration and low intrinsic electrical conductivity, and may explain the very low experimentally measured conductivity of bournonite by Bairamova et al.[21] We suggest that synthesis be attempted under Sb-poor conditions, where the formation energy of hole-killers is well above 0 eV (Sb_{Pb} in Figure 3-a).

There are a few possible ways, under equilibrium, to increase the hole concentrations and avoid the Fermi pinning issue[65] when it exists. First, we can extrinsically dope the compound with an acceptor that has a lower formation energy than the Sb_{Pb} defect. Second, we might attempt to move the absolute position of the VBM higher, bringing it closer to the position of the pinning level. Third, we may attempt to identify a substituted compound in which intrinsic *C* on *B* (donor) defect has a higher formation energy compared with acceptors while retaining stability and the same or better thermoelectric properties.

Regarding the first approach, we calculated the defects level of the following five candidates for extrinsic acceptors: In_{Pb}, Ge_{Sb}, Sn_{Sb}, P_S and As_S. The formation energies of these extrinsic defects at portions of the phase diagram, *i.e.*, for different chemical potentials, are available in Figures S9-S13. We find that none of the proposed acceptors possesses a lower energy than the hole killer Sb_{Pb}. However, it is possible that other extrinsic substitutional or interstitial dopants that we not evaluate could be more favorable.

Regarding the second mechanism, Cu/Ag hybridization with S/Se hybridization might be a way to push up the position of the valence band as discussed later. However, we did not attempt to evaluate absolute band positions in this work, *e.g.*, through explicit slab plus vacuum calculations.

Finally, we calculate the intrinsic defects formation energy of bournonite substitutions, in particular those of $CuPbSbSe_3$, $CuSnSbSe_3$ and $CuPbAsSe_3$ as presented in (Figure 3-b,c,d). While the shape of the defects levels in $CuPbSbS_3$ and $CuSnSbSe_3$ are similar, for $CuPbSbSe_3$ the intersection of dominant acceptor is Cu_{Pb} whereas for $CuSnSbSe_3$ it is Sn_{Sb}. For both materials, the intersection of the dominant acceptor with the hole killer (Sb on the *B* site) lies below or near the valence band, suggesting that *p*-type dopability should be comparable to the prototypical $CuPbSbS_3$ (or, for $CbPbSbSe_3$, perhaps a little more favorable). Here too, Sb-poor environments are recommended for the same reasons as in bournonite. However, Sb-poor environments are of particular importance in

$CuSnSbSe_3$ because this affects both the dominant acceptor and the hole killer. Discordantly, the $CuPbAsSe_3$ defect plot (Figure 3-d) indicates various acceptor defects such as V_{Pb}, V_{Cu} and Cu_{Pb} that are more favorable than the next most favorable hole killer, As_{Pb} by a large margin. Furthermore, Cu_{Pb} is already a shallow acceptor with a very low formation energy which may result in very large intrinsic hole concentrations in this material, which is desirable based on the transport calculations presented in Table 1.

Perhaps the most important limitation of the present defect analysis is the underestimation of the band gap by DFT, which is a well-known issue in predicting the correct defect levels.[66] One way of improving the analysis is to recalculate, at least for the most favorable donors/acceptors that we report, the energy levels using a hybrid functional. This may result in a lower formation energy of the Sb_{Pb} or Sn_{Pb} barriers against high doping levels. However, we expect that several conclusions are unlikely to change even with more accurate modeling, such as strong *p*-type tendencies of this group of compounds, which is also consistent with known *p*-type conductivity in similar Cu-S/Se materials (as we discuss more in Section 4).

3.2.3 Property trends with substitutions

We calculate various properties for each of the substitutions and compare them to see how each changes with substitutions along the same groups in the periodic table and whether they follow a pattern or a general "rule". As a first visualization, for a given property, we held a single element constant and plot the target property's value for each of all remaining combinations. For example, when examining formation energy, we might fix *A* = Na and plot formation energy values for all the 80 remaining *B, C, D* combinations. This type of visualization is presented in Supplementary Figure S14. This figure is helpful for examining raw data but is at too fine a resolution to visualize broad trends.

As a second visualization, for a given property, we hold a single element constant and *average* that property's value across all the remaining combinations of possible elements in other sites, as depicted in Figure 4. For example, we might fix *A* = Na and plot the *average* of values for the 80 remaining *B*, *C*, *D* combinations. Because there can be a high degree of variation in averaging the property values of many data points within diverse chemistries, data points in Figure 4 also include an "error bar" that represents the standard deviation of observations from the average.

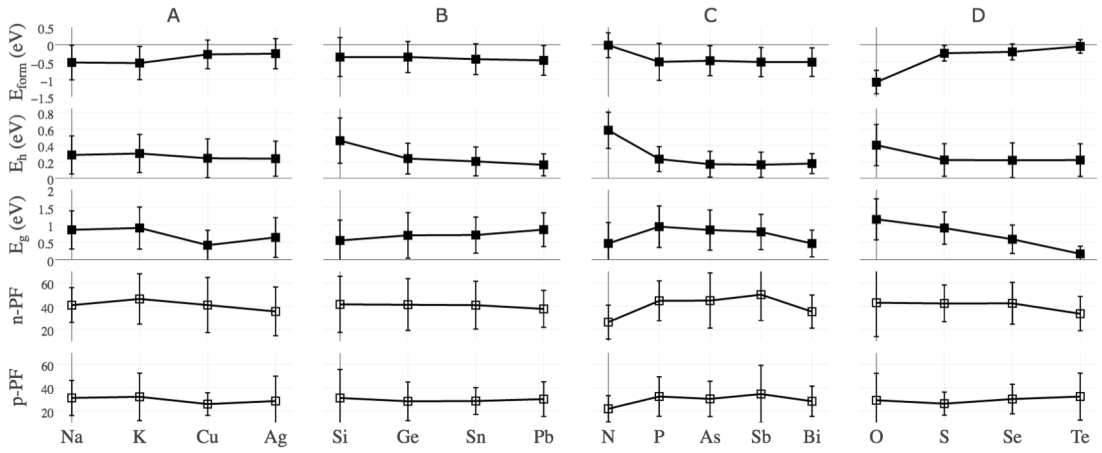

Figure 4. Overview of how elemental substitutions affect the several properties of bournonite. The average of the properties and their change within each group is plotted. The error bars indicate standard deviation in calculated values when one element is held fixed but others are allowed to vary. For *n*-PF and *p*-PF, the results are in the units of $\mu W/cm \cdot K^2$. Open symbols mean that not all data is available in the average, e.g., due to unconverged calculations. An analysis of trends is presented in the discussion.

We will analyze some of the trends from Figure 4 in the Discussion section. However, one aspect to note is the large standard deviations of the data points: even in cases where averaged properties follow clear trends when moving down a group in the periodic table, very large standard deviations indicate that holding a single element constant certainly does not tightly constrain the property values when given freedom of selection in the remaining elements.

Similarly, one can ask whether it is possible to tell whether a given property will increase or decrease if three of the elements in bournonite are held fixed and the remaining element is allowed to vary. As mentioned earlier, the raw data for to answer this question for specific systems can be visualized in Supplementary Figure S14. As a "coarse-grained" version of this question, we plot Figure 5 the tendency of several properties to increase or decrease when moving down the periodic table for a particular site while holding the other elements constant. For our analysis, each time that moving down a row in the periodic table for a given group increases the property value, we add 1 to a running sum, and each time this decreases the value, we subtract 1; the total sum is divided by the number of observations. This results in a scale of -1 (moving down a group always decreases the property, i.e., dark red points) to +1 (moving down a group always increases the property, i.e., dark blue points). For example, the darkest colors, and therefore the most reliable trends of increase/decrease when moving down a group, are for formation energies (apart from Na vs. K, which does not strongly affect the formation energy). We discuss these points more in Section 4.

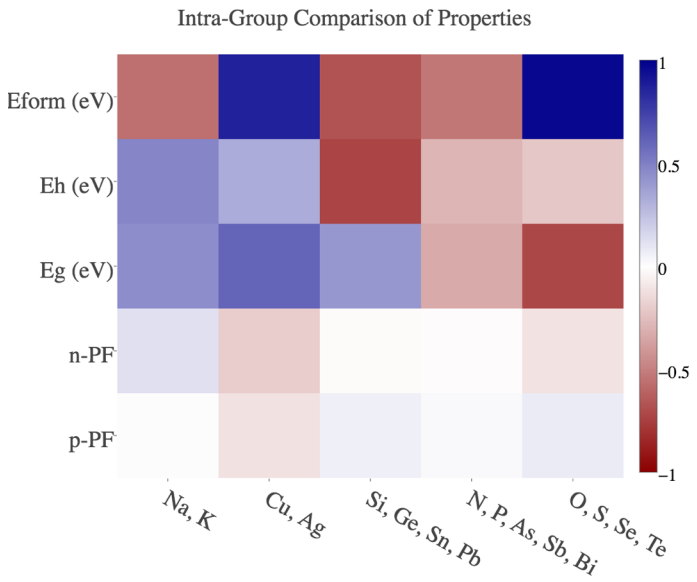

Figure 5. A visualization of trends in property changes of bournonite when substituting elements by moving down a group. The number of times that a property increases or decreases when we replace one element in $ABCD_3$ with a heavier element immediately lower (e.g. Si/Ge not Si/Sn) in the periodic table divided by the total number of comparisons presented in a scale -1 (always decreasing) to 1 (always increasing). Darker colors represent a more consistent change of that property, e.g., there is a strong tendency for band gaps to decrease for heavier anion (dark red for row E_g, column O, S, Se, Te). For more details, see the accompanying text.

4 Discussion

Using Figure 4 and Figure 5, we discuss broad trends in property values upon chemical substitution in the bournonite crystal structure. We first examine the formation energy, for which qualitative trends can be described fairly reliably. Figure 5 illustrates that moving down the periodic table almost always tends to increase the formation energy (i.e., less negative formation energies) for the *A* and *D* sites (dark blue) but decreases the formation energy for the *B* and *C* sites (medium to dark red). The exception is *A* = Na versus *A* = K, which has little effect on the formation energy on average. Because formation energies with respect to elements are not an important metric for the evaluation of thermoelectric compounds, such trends (even though they are strong) are not particularly useful from a technological standpoint.

A more relevant measure of the stability is the energy above hull, E_h, as described in Section 2.1. Because E_h is a more complex metric that evaluates decomposition into many different types of products, its trends with chemical substitution of a single element are not as dependable as for formation energy. This is confirmed by the lighter colors overall in Figure 5 for E_h versus E_{form}. However, despite individual differences, several major trends in stability can be observed. First, K-based compounds tend to be less stable

than Na-based compounds (despite their similarities in formation energy). As mentioned previously, this should be expected because K is a very large cation that makes it extremely difficult to retain the bournonite atomic arrangement. In all likelihood, both Na and K are too large to fit comfortably in the tetrahedral *A* site in bournonite: no compound for *A*=Na or *A*=K exhibits E_h < 0.050 eV/atom. The bournonite structure is much more robust for *A*=Cu or *A*=Ag, retaining its atomic structure 85% of the time for these elements overall (Figure S1) and with E_h as low as 0.001 eV/atom for *A*=Cu and 0.010 eV/atom for *A*=Ag. Regarding the *B* site, *B*=Si is essentially never stable in the bournonite structure (lowest E_h is 0.135 eV/atom). Common decomposition products (involved in more than 10 entries) include $SiSe_2$, SiS_2, SiO_2, and Si_3N_4; as may be expected, there is a strong tendency to decompose to compounds with Si in sp^3 hybridization rather than residing in a distorted 6- or 7-coordinated site within what would be a very unusual divalent, lone pair Si^{2+}. Even apart from the unstable nature of Si in bournonite, there is a further tendency for the bournonite structure to become more stable moving down the group for *B*-site atoms, *i.e.*, E_h decreases from Ge->Sn->Pb, as indicated by the red color in Figure 5 and as presented in Figure 4. This result is in-line with previous reports that the potential to form the divalent state increases going down the group from Ge to Sn to Pb.[67] A similar situation exists for the *C* site - the cation with the lowest Z (*C*=N^{3+}) is an unusual and unstable state (even the most stable N^{3+} compound in our study has E_h= 0.201 eV/atom). Apart from nitrogen, there is a broad trend of increasing stability with higher Z values (light red in Figure 5), although Sb appears to be more stable than Bi (some recent evidence suggests that Sb lone pairs are more favorable, at least within oxides, than Bi lone pairs[67]). In addition, the average stability of Sb- and As-containing substitutions is very similar, which is somewhat surprising given the difference between the chemistry of such compounds. Finally, for the *D* site, we find that oxide bournonites are generally unstable; they only retain the bournonite structure in 31% of substituted structures (Figure S1) and none have E_h < 0.050 eV/atom (although $NaAsPbO_3$, with E_h = 0.051 eV/atom, comes close). For the other choices of *D* (S, Se, Te), Figure 4 reveals that the *average* stability is similar. However, when examining the most stable compounds, all compounds that have E_h < 0.010 eV/atom are sulfides, and all compounds with E_h < 0.049 eV/atom are either sulfides or selenides. Thus, it appears that forming a stable bournonite is easier in sulfides and selenides than in tellurides. It is possible that this trend can be rationalized by work from Walsh et al.[67] demonstrating that the positions of anionic levels strongly affect the potential of cations to form stereochemically active lone pairs. Within this perspective, the *p* states of only the more electronegative anions (e.g., sulfur) are deep enough to mix with cation *s* states. This mixing results in antibonding states that can subsequently interact with cation *p*-states, stabilizing the stereochemically active lone pair state. This interpretation would explain why we do not have any tellurides in our list of most stable

compounds. However, it does not explain the issues with retaining the bournonite structure in oxides, which is likely due to other factors such as the size of the anion.

Next we examine the band gap. We note that band gaps in GGA are systematically underestimated[49,50] such that the quantitative value of the results are likely incorrect; however, the qualitative trends should be reliable (an exception is that non spin-orbit coupling calculation can sometimes overestimate the band gap for systems with strong spin-orbit coupling). Figure 4 and Figure 5 clearly depict a well-known trend that band gaps decrease when the anion is exchanged for a larger, less electronegative one (*i.e.*, decreases from oxides to tellurides) due to increased covalency and reduced ionicity as well as increasing cell volumes, in-line with tight-binding theory[24]. A similar effect may explain the larger band gaps of Na and K versus Cu and Ag (Figure 4), although this comparison is likely complicated by the fact that the final atomic arrangements of Na and K atoms in our calculations are not always of "bournonite type", as discussed previously. Overall, for elements that tend to be relatively stable in bournonite (i.e., excluding Na, K, Si, N, and O), there appear to be two broad groups of compounds: large unit cells with relatively low electronegativity differences (>725 A^3 cells with standard deviation of electronegativity <0.2) and smaller unit cells with medium electronegativity differences (<725 A^3 cells with standard deviation of electronegativity >0.2). For the former group, the average band gap is only 0.08 eV whereas for the latter group, the average band gap is 0.63 eV. Thus, electronegativity and size clearly play a large role, although there exists significant scatter in band gap values within each group, suggesting that size and electronegativity are certainly not the only important factors (see Supplementary Figure S3).

Another trend is that band gaps for silver-based compounds are typically larger than those for copper-based compounds, despite (i) copper and silver have very similar Pauling electronegativities and (ii) silver is the larger cation, and larger volumes typically reduce the gap. We believe that this trend is due to Cu^+ *d*-states lying higher in the valence band than Ag^+ *d*-states, and indeed lying higher than the anionic *p*-states of O, S, and Se. The projected density of states (DOS) for $CuPbSbS_3$ plotted in Figure 6 confirms that the contribution of Cu^+ *d*-states to the valence band is larger than that of S^{2-} *p*-states. Even for the selenide ($CuPbSbSe_3$), the DOS projection for Cu^+ *d*-states is higher than that of the anion. This is in contrast to Ag^+, for which we find that both Se^2 and S^{2-} anion states contribute slightly more to the valence band than Ag^+. We note that these band edge trends are consistent with a previous data mining study that we performed on the contributions of different ions to the valence and conduction bands of materials[68]. The band structure of $CuPbSbS_3$ calculated via GGA+*U* (*U*=3.0 as a test) has the same characteristic of Cu-*d* states vs. S and Se *p* states in the valence band (though the band gap increases as expected, see Figure S5). Thus, the band gap of Cu-containing compounds is reduced to due to the high position in the valence band of Cu^+.

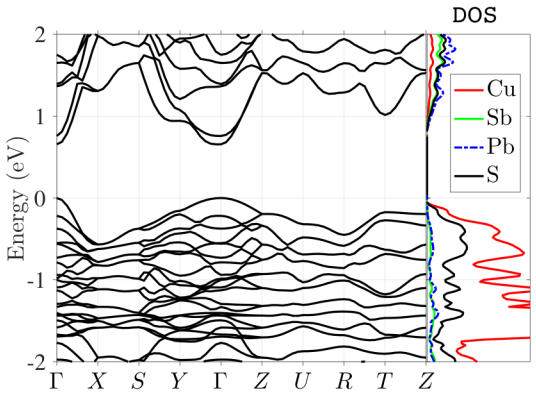

Figure 6. The band structure and atom-projected density of states of $CuPbSbS_3$. See Figures S2-S4 for projected band structures of selected compounds as well as those calculated with spin orbit coupling for selected compounds.

The band gap for the *B* and *C* cation sites demonstrate opposite trends (Figure 5): whereas the gap tends to increase with larger *B* site ions, it tends to decrease with larger *C* site ions (with the exception of *C*=N, which is an outlier). The reasons underpinning these trends are unclear; although increasing the size of a cation often reduces the band gap due to increased cell volume and separation between atoms, the opposite effect can also occur in systems with lone pair electrons[24] such as the *B* and *C* sites of bournonite.

Although Figure 4 and Figure 5 indicate no strong trends in the power factors, one interesting observation can be made about the standard deviation of power factors as indicated by the "error bars" in Figure 4. For *n*-type calculated power factors, all standard deviations are relatively large, showing that holding any single element constant does not constrain the power factor to a great degree. However, for *p*-type power factors, the range of calculated power factors is smaller for Cu, S, and Se. This is consistent with our earlier statements that these three elements tend to dominate the valence band edge when present, and thus constraining these elements is more likely to "pin" the power factor at a particular value. In contrast, the conduction band is formed by a mix of all elemental states and is more difficult to assign to a single element.

In addition to the band structure and density of states (DOS) plotted in Figure 6, we also calculated the band structure and power factors of some substitutions taking spin orbit coupling (SOC) interactions into account. The band structure plotted in Figure 6 agrees well with that previously reported by Dong et al.[23]: 0.69 eV direct gap which is equal to what we calculate (Table 1). Furthermore, the SOC interaction (Figure S4) reduces the band gap and shifts the position of the CBM to lie between the Y and Γ points, making the gap indirect, also consistent with the previous results of Dong et al[23]. We note that including SOC mainly affects the conduction band, such that *p*-type properties are largely unaffected by SOC. For $CuPbSbS_3$ and $CuPbAsS_3$, our calculated *p*-PF were equal within

0.1 μW/cm·K^2 with or without SOC. For $CuSnSbSe_3$, *p*-PF with SOC included is 5.5% higher, which is somewhat significant but still small enough to justify comparisons between calculated *p*-type power factors without including SOC.

We explain some of the transport calculation results further examining the band structures and the parameters used in the calculations. First, we note that, apart from two exceptions out of ten that we discuss later ($CuSnSbS_3$ and $CuSnAsS_3$), the AMSET and BoltzTraP results agree well in terms of qualitative trends (Figure 7). In addition, it is possible to use the AMSET results to determine an "equivalent" BoltzTraP relaxation time of $\tau = 4.0\times10^{-14}$ seconds that results in similar quantitative predictions between AMSET and BoltzTrap (blue line, Figure 7).

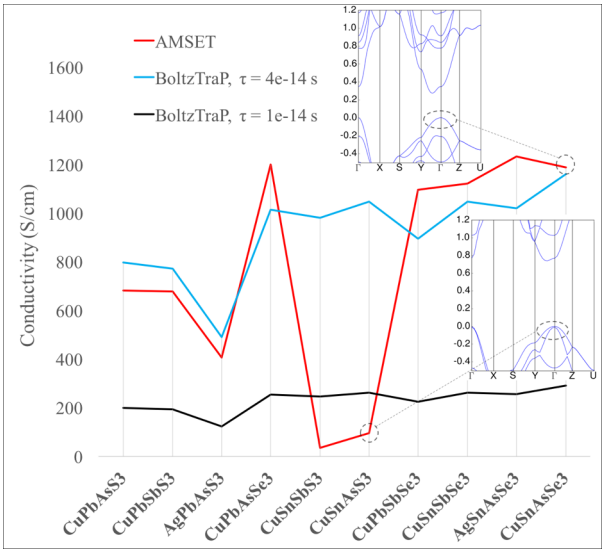

Figure 7. Calculated conductivity via AMSET (red), BoltzTrap with $\tau = 1.0\times10^{-14}$s relaxation time (black), and BoltzTraP with $\tau = 4.0\times10^{-14}$ (red). Data is shown for the ten most stable substitutions reported in Table 1. The AMSET conductivity for $CuSnSbS_3$ and $CuSnAsS_3$ is low due to the presence of inter-band scattering, as shown by the inset band structure diagrams that illustrate valence band degeneracy for CuSnAsS3. Calculated Seebeck coefficients are available in the Figure S15.

One trend in the transport results is that the AMSET-calculated *p*-PF* increases when S is substituted by Se. Selenium more strongly participates in the valence band (See Figure S2) reducing the hole effective mass, m_h^* through increased hybridization (m_h^*=1.0 for S and 0.78 for Se). In the AMSET model, replacement of sulfur with selenium results in a small detrimental effect on the Seebeck coefficient (178 $\mu V/K$ for $CuPbSbS_3$ to 159 $\mu V/K$ for $CuPbSbSe_3$) but also a much stronger positive effect on the mobility from 42 to 68 cm^2/V·s. This effect originates from both the ionized impurity and longitudinal optical (LO) phonon scattering being weaker for $CuPbSbSe_3$ than $CuPbSbS_3$. In particular, the LO phonon mobility is 61 cm^2/V·s in $CuPbSbS_3$ while it is 95 cm^2/V·s for $CuPbSbSe_3$.

The same arguments hold true when we compare the properties of $CuPbSbS_3$ vs. $CuSnSbSe_3$ (i.e., Pb->Sn and S->Se). The AMSET Seebeck coefficient for $CuSnSbSe_3$ is almost unchanged (175 $\mu V/K$) while the mobility is again significantly improved (69 $cm^2/V{\cdot}s$, limited by LO phonon = 109 $cm^2/V{\cdot}s$).

We also note that AMSET calculations of two compounds in Figure 7 exhibit anomalously low power factors. For example, even though it might be expected that $CuSnSbSe_3$ would possess similar electronic properties to $CuSnSbS_3$, we see that the AMSET predicted *p*-PF drops significantly. A close look at the band structures of these two compounds (Figure 7 insets) reveals that the $CuSnSbS_3$ valence band is degenerate, which facilitates inter-band scattering of the top two degenerate valence bands in the coupled-band transport model[51] implemented in AMSET and significantly reduces the overall hole mobility (down to 2 $cm^2/V{\cdot}s$). A similar situation occurs in our calculation for $CuSnAsS_3$. We note that these inter-band effects may be overestimated in AMSET and further investigation may be necessary. For example, for 3% Na-doped p-type Ca_3AlSb_3, Zevalkink et al.[69] reported a measured PF of 3 $\mu W/cm{\cdot}K^2$ at $c = 1.1{\times}10^{19}$ cm^{-3} whereas we calculated the p-PF* for this material equal to 0.85 $\mu W/cm{\cdot}K^2$, with the underestimation most likely due to an overestimation of the interband scattering in the heavy and light hole that reduced our conductivity prediction (12 S/cm calculated vs. 60 S/cm measured). Furthermore, we note that neither of our models explicitly considers the possibility of polaronic effects, which would reduce the conductivity from the values reported in this paper.

Our defect calculations revealed that *n*-type bournonite compounds are unlikely to be achieved. This has been observed in many p-type Cu-S based materials such as Cu_3SbSe_4[12,13], Cu_2ZnSnS_4[70], Cu-alloyed ZnS[71], or $CuGaSe_2$[65] with different levels of Cu-S (or Se) hybridization (Figure 6). Because the barriers to forming *p*-type materials are not too high, it may be possible to introduce extrinsic defects that form a high concentration of holes or in the case of $CuPbAsSe_3$ have a high intrinsic hole concentration. In addition, our calculations reveal that Sb-poor synthesis conditions may facilitate *p*-type doping in Sb-containing bournonite substitutions. We note that a recent study by Tamaki et al. on Mg_3Sb_2 observed that even small changes to stoichiometry can have outsize effects on doping and thermoelectric properties,[72] suggesting that such experiments may be worthy of future study. Furthermore, we calculated that the hole killer levels in both $CuPbSbSe_3$ and $CuSnSbSe_3$ relative to the VBM are higher than in the prototypical $CuPbSbS_3$ such that these substitutions may be promising new materials. It should be noted that these results would be more clearly confirmed by employing a hybrid functional (*e.g.*, HSE[73]). However, we hope that this study will be helpful to guide thermoelectric researchers toward designing high efficiency earth abundant natural minerals (specifically bournonites) to be used in thermoelectric applications.

5 Conclusions

We have employed first-principles calculations to evaluate several properties of 320 substitutions into the bournonite structure. We evaluated optimized structures (including cell volumes and whether they retain a bournonite arrangement), E_{form}, E_h, E_g, σ, α, power factor, and defect properties. Based on these calculations, we find that $CuPbSbSe_3$, $CuSnSbSe_3$ and $CuPbAsSe_3$ may be interesting candidates for further study. Particularly $CuPbAsSe_3$ possess excellent defect and transport properties. Furthermore, we analyze and explain the defect behavior of these materials, including their strong *p*-type dependencies. We also compare two different models of transport and demonstrate how calculating scattering effects can be used both to determine an equivalent relaxation time as well as to account for inter-band scattering. Finally, we explained trends in the stability and band gap of these materials with chemical substitution. In particular, we note that bournonite atomic arrangement is not always retained upon structural optimization, and that lone pair effects may be important in stabilizing the desired arrangement. Thus, our study suggests both specific compound candidates as well as new insights that can be used to guide the exploration of bournonite-type materials.

ASSOCIATED CONTENT

Supplementary Information

The Supplementary Information is available free of charge. The following has been provided as Supplementary Information:

bournonite_exploration.PDF: Figures: band structures with orbital projections and spin orbit coupling and band gap statistics. Heatmap plots of fraction of susbtitutions that retain bournonite type structures + Defects plots + detailed plots for tracking individual properties/material and more.

bournonite_exploration.xlsx: containing complete data for all the substitutions and their lattice constants, band gap, E above hull, transport properties calculated by Boltztrap and AMSET and their corresponding doping level and temperature, calculated coordination numbers, list of compounds for which DFT band gap is zero.

AUTHOR INFORMATION

Corresponding Author

* E-mail: alireza.faghaninia@gmail.com, ajain@lbl.gov

ACKNOWLEDGEMENTS

This work was intellectually led by U.S. Department of Energy, Office of Basic Energy Sciences, Early Career Research Program. GH GMR and GY acknowledge the F.R.S.-

FNRS project HTBaSE (contract nº PDR-T.1071.15) for financial support. UA, MW and GJS acknowledge the Materials Project as a funding source, which is supported by the Department of Energy Basic Energy Sciences program under Grant No. EDCBEE, DOE Contract DE-AC02- 05CH11231. This research used resources of the National Energy Research Scientific Computing Center (NERSC), a DOE Office of Science User Facility supported by the Office of Science of the U.S. Department of Energy. Additional computational resources have been provided by the supercomputing facilities of the Université catholique de Louvain (CISM/UCL), the Consortium des Equipements de Calcul Intensif en Federation Wallonie Bruxelles de (CECI) funded by the F.R.S.-FNRS, and the Tier-1 supercomputer of the Fédération Wallonie-Bruxelles, infrastructure funded by the Walloon Region under the grant agreement number 1117545. We also thank Cynthia Lo for additional computing support, in particular for AMSET calculations.

We thank Saurabh Bajaj for helpful discussions and his support in generating the plots using the FigRecipes codes available online under https://github.com/hackingmaterials/matminer. We thank Francesco Ricci for his help with the BoltzTraP calculations. We thank Shyue Ping Ong, William Davidson Richards, and David Waroquiers for their efforts on the pymatgen software and development of the StructureMatcher and ChemEnv tools.

ABBREVIATIONS

A: group of elements in $ABCD_3$ structure: {Na-K-Cu-Ag}
B: group of elements in $ABCD_3$ structure: {Si-Ge-Sn-Pb}
C: group of elements in $ABCD_3$ structure: {N-P-As-Sb-Bi}
D: group of elements in $ABCD_3$ structure: {O-S-Se-Te}
X: Pauling electronegativity
CN: coordination number
E_{form}: formation energy per atom (eV/atom)
E_{df}: formation energy of a defect (eV)
E_F: Fermi level (eV)
E_h: energy above hull (eV/atom)
E_g: band gap (eV)
n-PF: maximum n-type power factor
p-PF: maximum p-type power factor
c: carrier concentration (cm^{-3})

1 T. M. Tritt and M. A. Subramanian, Thermoelectric Materials, Phenomena, and Applications : A Bird's Eye View, *MRS Bull.*, 2006, **31**, 188–198.

2 C. A. Gould, N. Y. A. Shammas, S. Grainger and I. Taylor, Thermoelectric Cooling of Microelectronic Circuits and Waste Heat Electrical Power Generation in a Desktop Personal Computer, *Mater. Sci. Eng. B*, 2011, **176**(4), 316–325.

3 A. P. Gonçalves and C. Godart, New Promising Bulk Thermoelectrics: Intermetallics, Pnictides and Chalcogenides, *Eur. Phys. J. B*, 2014, **87**(42).

4 G. J. Snyder and E. S. Toberer, Complex Thermoelectric Materials, *Nat. Mater.*, 2008, **7**, 105–114.

5 C. Candolfi, U. Aydemir, A. Ormeci, W. Carrillo-Cabrera, U. Burkhardt, M. Baitinger, N. Oeschler, F. Steglich and Y. Grin, Transport Properties of the Clathrate BaGe5, *J. Appl. Phys.*, 2011, **110**, 43715.

6 X. Shi, J. Yang, J. R. Salvador, M. Chi, J. Y. Cho, H. Wang, S. Bai, J. Yang, W. Zhang and L. Chen, Multiple-Filled Skutterudites: High Thermoelectric Figure of Merit through Separately Optimizing Electrical and Thermal Transports, *J. Am. Chem. Soc.*, 2011, **133**(20), 7837–7846.

7 U. Aydemir, A. Zevalkink, A. Ormeci, S. Bux and G. J. Snyder, Enhanced Thermoelectric Properties of the Zintl Phase $BaGa_2Sb_2$ via Doping with Na or K, *J. Mater. Chem. A*, 2016, **4**(5), 1867–1875.

8 S. M. Kauzlarich, S. R. Brown and G. J. Snyder, Zintl Phases for Thermoelectric Devices., *Dalton Trans.*, 2007(21), 2099–2107.

9 U. Aydemir, J.-H. Pöhls, H. Zhu, G. Hautier, S. Bajaj, Z. M. Gibbs, W. Chen, G. Li, S. Ohno, D. Broberg, S. D. Kang, M. Asta, G. Ceder, M. A. White, K. Persson, A. Jain and G. J. Snyder, $YCuTe_2$: A Member of a New Class of Thermoelectric Materials with $CuTe_4$-Based Layered Structure, *J. Mater. Chem. A*, 2016, **4**(7), 2461–2472.

10 H. Zhu, G. Hautier, U. Aydemir, Z. M. Gibbs, G. Li, S. Bajaj, J.-H. Pöhls, D. Broberg, W. Chen, A. Jain, M. A. White, M. Asta, G. J. Snyder, K. Persson and G. Ceder, Computational and Experimental Investigation of $TmAgTe_2$ and XYZ_2 Compounds, a New Group of Thermoelectric Materials Identified by First-Principles High-Throughput Screening, *J. Mater. Chem. C*, 2015, **3**, 10554–10565.

11 S. D. Kang, S. A. Danilkin, U. Aydemir, M. Avdeev, A. Studer and G. J. Snyder, Apparent Critical Phenomena in the Superionic Phase Transition of $Cu_{2-x}Se$, *New J. Phys.*, 2016, **18**, 13024.

12 E. J. Skoug, J. D. Cain and D. T. Morelli, High Thermoelectric Figure of Merit in the Cu_3SbSe_4-Cu_3SbS_4 Solid Solution, *Appl. Phys. Lett.*, 2011, **98**(26), 261911.

13 T.-R. Wei, Z. M. Wang, Heng, Gibbs, C.-F. Wu, G. J. Snyder and J.-F. Li, Thermoelectric Properties of Sn-Doped P-Type Cu_3SbSe_4 : A Compound with Large Effective Mass and Small Band Gap, *J. Mater. Chem. A*, 2014, **2**(33), 13527–13533.

14 L. Li, Y. Liu, J. Dai, A. Hong, M. Zeng, Z. Yan, J. Xu, D. Zhang, D. Shan, S. Liu, Z. Ren and J. M. Liu, High Thermoelectric Performance of Superionic Argyrodite Compound Ag_8SnSe_6, *J. Mater. Chem. C*, 2016, **4**(24), 5806–5813.

15 P. F. Qiu, T. S. Zhang, Y. T. Qiu, X. Shi and L. D. Chen, Sulfide Bornite Thermoelectric Material: A Natural Mineral with Ultralow Thermal Conductivity, *Energy Environ. Sci.*, 2014, **7**, 4000–4006.

16 X. Lu and D. T. Morelli, Natural Mineral Tetrahedrite as a Direct Source of Thermoelectric Materials., *Phys. Chem. Chem. Phys.*, 2013, **15**(16), 5762–5766.

17 K. Suekuni, F. S. Kim, H. Nishiate, M. Ohta, H. I. Tanaka and T. Takabatake, High-Performance Thermoelectric Minerals: Colusites $Cu_{26}V_2M_6S_{32}$ (M = Ge, Sn), *Appl. Phys. Lett.*, 2014, **105**(13), 132107.

18 X. Lu, D. T. Morelli, Y. Xia, F. Zhou, V. Ozolins, H. Chi, X. Zhou and C. Uher, High Performance Thermoelectricity in Earth-Abundant Compounds Based on Natural Mineral Tetrahedrites, *Adv. Energy Mater.*, 2013, **3**(3), 342–348.

19 K. S. Weldert, W. G. Zeier, T. W. Day, M. Panthöfer, G. J. Snyder and W. Tremel, Thermoelectric Transport in Cu_7PSe_6 with High Copper Ionic Mobility, *J. Am. Chem. Soc.*, 2014, **136**(34), 12035–12040.

20 A. Edenharter and W. Nowacki, Verfeinerung Der Kristallstruktur von Bournonit $[(SbS_3)_2|Cu_2^{IV}Pb^{VII}Pb^{VIII}]$ Und von Seligmannit $[(AsS_3)_2|Cu_2^{IV}Pb^{VII}Pb^{VIII}]$, *Zeitschrift für Krist.*, 1970, **131**, 397–417.

21 S. T. Bairamova, M. R. Bagieva, S. M. Agapashaeva and O. M. Aliev, Synthesis and Properties of Structural Analogs of the Mineral Bournonite, *Inorg. Mater.*, 2011, **47**(4), 345–348.

22 K. Wei, J. Martin, J. R. Salvador and G. S. Nolas, Synthesis and Characterization of Bournonite $PbCuSbS_3$ Nanocrystals, *Crys. Growth Des.*, 2015, **15**(8), 3762–3766.

23 Y. Dong, A. R. Khabibullin, K. Wei, J. R. Salvador, G. S. Nolas and L. M. Woods, Bournonite $PbCuSbS_3$: Stereochemically Active Lone-Pair Electrons That Induce Low Thermal Conductivity, *ChemPhysChem*, 2015, **16**(15), 3264–3270.

24 W. G. Zeier, A. Zevalkink, Z. M. Gibbs, G. Hautier, M. G. Kanatzidis and G. J. Snyder, Thinking Like a Chemist : Intuition in Thermoelectric Materials, *Angew. Chemie Int. Ed.*, 2016, **55**(24), 6826–6841.

25 H. Luo, J. W. Krizan, L. Muechler, N. Haldolaarachchige, T. Klimczuk, W. Xie, M. K. Fuccillo, C. Felser and R. J. Cava, A Large Family of Filled Skutterudites Stabilized by Electron Count, *Nat. Commun.*, 2015, **6**, 6489.

26 J. Zhang, L. Song, G. K. H. Madsen, K. F. F. Fischer, W. Zhang, X. Shi and B. B. Iversen, Designing High-Performance Layered Thermoelectric Materials through Orbital Engineering, *Nat. Commun.*, 2016, **7**, 10892.

27 T. D. Sparks, M. W. Gaultois, A. Oliynyk, J. Brgoch and B. Meredig, Data Mining Our Way to the next Generation of Thermoelectrics, *Scr. Mater.*, 2016, **111**, 10–15.

28 J. Yan, P. Gorai, B. Ortix, S. Miller, S. A. Barnett, T. Mason, V. Stevanovic and E. S. Toberer, Material Descriptors for Predicting Thermoelectric Performance, *Energy Enviornmental Sci.*, 2015, **8**(3), 983–994.

29 W. Chen, J. Po, G. Hautier, D. Broberg, S. Bajaj, U. Aydemir, Z. M. Gibbs, H. Zhu, M. Asta, G. J. Snyder, B. Meredig and A. White, Understanding Thermoelectric Properties from High-Throughput Calculations: Trends, Insights, and Comparisons with Experiment, *J. Mater. Chem. C*, 2016, **4**(20), 4414–4426.

30 A. O. Oliynyk, E. Antono, T. D. Sparks, L. Ghadbeigi, M. W. Gaultois, B. Meredig and A. Mar, High-Throughput Machine-Learning-Driven Synthesis of Full-Heusler Compounds, *Chem. Mater.*, 2016, **28**(20), 7324–7331.

31 G. K. H. Madsen, Automated Search for New Thermoelectric Materials: The Case of LiZnSb, *J. Am. Chem. Soc.*, 2006, **128**(37), 12140–12146.

32 S. Wang, Z. Wang, W. Setyawan, N. Mingo and S. Curtarolo, Assessing the Thermoelectric Properties of Sintered Compounds via High-Throughput Ab-Initio Calculations, *Phys. Rev. X*, 2011, **1**, 21012.

33 J. Carrete, W. Li, N. Mingo, S. Wang and S. Curtarolo, Finding Unprecedentedly Low-Thermal-Conductivity Half-Heusler Semiconductors via High-Throughput Materials Modeling, *Phys. Rev. X*, 2014, **4**, 11019.

34 P. Gorai, P. Parilla, E. S. Toberer and V. Stevanović, Computational Exploration of the Binary A_1B_1 Chemical Space for Thermoelectric Performance, *Chem. Mater.*, 2015, **27**(18), 6213–6221.

35 P. Gorai, D. Gao, B. Ortiz, S. Miller, S. A. Barnett, T. Mason, Q. Lv, V. Stevanović and E. S. Toberer, TE Design Lab: A Virtual Laboratory for Thermoelectric Material Design, *Comput. Mater. Sci.*, 2016, **112**, 368–376.

36 K. F. Garrity, First-Principles Search for N -Type Oxide, Nitride, and Sulfide Thermoelectrics, *Phys. Rev. B - Condens. Matter Mater. Phys.*, 2016, **94**(4), 1–11.

37 G. K. H. Madsen and D. J. Singh, BoltzTraP. A Code for Calculating Band-Structure Dependent Quantities, *Comput. Phys. Commun.*, 2006, **175**(1), 67–71.

38 A. Faghaninia, C. S. Lo and J. W. Ager, Ab Initio Electronic Transport Model with Explicit Solution to the Linearized Boltzmann Transport Equation, *Phys. Rev. B*, 2015, **91**(23), 5100.

39 G. Kresse and J. Furthmüller, Efficient Iterative Schemes for Ab Initio Total-Energy Calculations Using a Plane-Wave Basis Set, *Phys. Rev. B*, 1996, **54**(16), 11169–11186.

40 G. Kresse and J. Furthmüller, Efficiency of Ab-Initio Total Energy Calculations for Metals and Semiconductors Using a Plane-Wave Basis Set, *Comput. Mater. Sci.*, 1996, **6**(1), 15–50.

41 J. P. Perdew, K. Burke and M. Ernzerhof, Generalized Gradient Approximation Made Simple, *Phys. Rev. Lett.*, 1996, **77**(18), 3865–3868.

42 P. E. Blöchl, Projector Augmented-Wave Method, *Phys. Rev. B*, 1994, **50**(24), 17953–17979.

43 G. Kresse and D. Joubert, From Ultrasoft Pseudopotentials to the Projector Augmented-Wave Method, *Phys. Rev. B*, 1999, **59**(3), 1758–1775.

44 A. Jain, S. Ping Ong, W. Chen, B. Medasani, X. Qu, M. Kocher, M. Brafman, G. Petretto, G.-M. Rignanese, G. Hautier, D. Gunter and K. A. Persson, FireWorks: A Dynamic Workflow System Designed for Highthroughput Applications, *Concurr. Comput. Pract. Exp.*, 2015, **27**, 5037–5059.

45 S. P. Ong, W. D. Richards, A. Jain, G. Hautier, M. Kocher, S. Cholia, D. Gunter, V. L. Chevrier, K. A. Persson and G. Ceder, Python Materials Genomics (Pymatgen): A Robust, Open-Source Python Library for Materials Analysis, *Comput. Mater. Sci.*, 2013, **68**, 314–319.

46 A. Jain, S. P. Ong, G. Hautier, W. Chen, W. D. Richards, S. Dacek, S. Cholia, D. Gunter, D. Skinner, G. Ceder and K. A. Persson, Commentary: The Materials Project: A Materials Genome Approach to Accelerating Materials Innovation, *APL Mater.*, 2013, **1**(1), 11002.

47 G. Hautier, S. P. Ong, A. Jain, C. J. Moore and G. Ceder, Accuracy of Density Functional Theory in Predicting Formation Energies of Ternary Oxides from Binary Oxides and Its Implication on Phase Stability, *Phys. Rev. B*, 2012, **85**, 155208.

48 W. Sun, S. T. Dacek, S. P. P. Ong, G. Hautier, A. Jain, W. Richards, A. C. Gamst, K. A. A. Persson and G. Ceder, The Thermodynamic Scale of Inorganic Crystalline Metastability, *Sci. Adv.*, 2016, **2**(11), e1600225.

49 J. P. Perdew and M. Levy, Physical Content of the Exact Kohn-Sham Orbital Energies: Band Gaps and Derivative Discontinuities, *Phys. Rev. Lett.*, 1983, **51**(20), 1884–1887.

50 L. J. Sham and M. Schlüter, Density-Functional Theory of the Energy Gap, *Phys. Rev. Lett.*, 1983, **51**(20), 1888–1891.

51 A. T. Ramu, L. E. Cassels, N. H. Hackman, H. Lu, J. M. O. Zide and J. E. Bowers, Thermoelectric Transport in the Coupled Valence-Band Model, *J. Appl. Phys.*, 2011, **109**(3), 33704.

52 B. W. Kim and A. Majerfeld, Two Band Analysis of Hole Mobility and Hall Factor for Heavily Carbon Doped P-Type GaAs, *J. Appl. Phys.*, 1996, **79**(4), 1939–1950.

53 E. J. Skoug and D. T. Morelli, Role of Lone-Pair Electrons in Producing Minimum Thermal Conductivity in Nitrogen-Group Chalcogenide Compounds, *Phys. Rev.*

Lett., 2011, **107**(23), 235901.

54 A. Togo and I. Tanaka, First Principles Phonon Calculations in Materials Science, *Scr. Mater.*, 2015, **108**, 1–5.

55 I. Petousis, W. Chen, G. Hautier, T. Graf, T. D. Schladt, K. A. Persson and F. B. Prinz, Benchmarking Density Functional Perturbation Theory to Enable High-Throughput Screening of Materials for Dielectric Constant and Refractive Index, *Phys. Rev. B*, 2016, **93**, 115151.

56 T. Le Bahers, M. Rérat and P. Sautet, Semiconductors Used in Photovoltaic and Photocatalytic Devices: Assessing Fundamental Properties from DFT, *J. Phys. Chem. C*, 2014, **118**(12), 5997–6008.

57 R. H. Lyddane, R. G. Sachs and E. Teller, On the Polar Vibrations of Alkali Halides, *Phys. Rev.*, 1941, **59**, 673–676.

58 D. L. Rode, Low-Field Electron Transport, *elsevier*, 1975, vol. 10.

59 C. Freysoldt, B. Grabowski, T. Hickel, J. Neugebauer, G. Kresse, A. Janotti and C. G. Van De Walle, First-Principles Calculations for Point Defects in Solids, *Rev. Mod. Phys.*, 2014, **86**(1), 253–305.

60 C. Freysoldt, J. Neugebauer and C. G. Van De Walle, Fully Ab Initio Finite-Size Corrections for Charged-Defect Supercell Calculations, *Phys. Rev. Lett.*, 2009, **102**(1), 16402.

61 Y. Kumagai and F. Oba, Electrostatics-Based Finite-Size Corrections for First-Principles Point Defect Calculations, *Phys. Rev. B*, 2014, **89**(195205).

62 O. L. Kheifets, L. Y. Kobelev, N. V. Melnikova and L. L. Nugaeva, Electrical Properties of Solid Electrolytes with the General Formula $ABCD_3$ (A = Ag, Cu; B = Pb, Sn; C = As, Sb; and D = S, Se), *Tech. Phys.*, 2007, **52**(1), 86–92.

63 O. Kheifets, N. Melnikova, L. Saypulaeva, A. Alibekov, A. Mollaev, A. Babushkin and G. Tikhomirova, Electric Properties of $AgPbAsSe_3$ at Pressures up to 45 GPa, *High Press. Res.*, 2009, **29**(2), 261–266.

64 S. Kharbish, G. Giester and A. Beran, Contribution to the Crystal Structures of Tennantite and Bournonite, *Neues Jahrb. für Mineral. - Abhandlungen*, 2010, **187**(2), 159–166.

65 A. Zunger, Practical Doping Principles, *Appl. Phys. Lett.*, 2003, **83**(1), 57–59.

66 A. Janotti and C. G. Van de Walle, LDA + U and Hybrid Functional Calculations for Defects in ZnO, SnO2, and TiO2, *Phys. Status Solidi B*, 2011, **248**(4), 799–804.

67 A. Walsh, D. J. Payne, R. G. Egdell and G. W. Watson, Stereochemistry of Post-Transition Metal Oxides: Revision of the Classical Lone Pair Model., *Chem. Soc.*

Rev., 2011, **40**(9), 4455–4463.

68 A. Jain, G. Hautier, S. P. Ong and K. Persson, New Opportunities for Materials Informatics: Resources and Data Mining Techniques for Uncovering Hidden Relationships, *J. Mater. Res.*, 2016, **31**(8), 977–994.

69 A. Zevalkink, E. S. Toberer, W. G. Zeier, E. Flage-larsen and G. J. Snyder, Ca_3AlSb_3: An Inexpensive, Non-Toxic Thermoelectric Material for Waste Heat Recovery, *Energy Environ. Sci.*, 2011, **4**, 510–518.

70 S. Chen, J. H. Yang, X. G. Gong, A. Walsh and S. H. Wei, Intrinsic Point Defects and Complexes in the Quaternary Kesterite Semiconductor Cu_2ZnSnS_4, *Phys. Rev. B*, 2010, **81**, 245204.

71 R. Woods-Robinson, J. K. Cooper, X. Xu, L. T. Schelhas, V. L. Pool, A. Faghaninia, C. S. Lo, M. F. Toney, I. D. Sharp and J. W. Ager, P-Type Transparent Cu-Alloyed ZnS Deposited at Room Temperature, *Adv. Electron. Mater.*, 2016, **2**(6), 1500396.

72 H. Tamaki, H. K. Sato and T. Kanno, Isotropic Conduction Network and Defect Chemistry in $Mg_{3+\delta}Sb_2$-Based Layered Zintl Compounds with High Thermoelectric Performance, *Adv. Mater.*, 2016, **28**(46), 10182–10187.

73 J. Heyd, G. E. Scuseria and M. Ernzerhof, Hybrid Functionals Based on a Screened Coulomb Potential, *J. Chem. Phys.*, 2003, **118**(18), 8207–8215.